Research Square

Preprints are preliminary reports that have not undergone peer review.
They should not be considered conclusive, used to inform clinical practice,
or referenced by the media as validated information.

A Computational Framework for Predicting the Mechanical Properties of Recycled CFRP Laminates

Ilektra Tourkantoni
University of Patras
Konstantinos Tserpes
kitserpes@upatras.gr
University of Patras

Research Article

Keywords: Plasma-assisted solvolysis, CFRP remanufacturing, Micromechanical analysis, Multi-scale modelling, Finite element analysis

Posted Date: November 23rd, 2026

DOI: https://doi.org/10.21203/rs.3.rs-11480087/v1

License: This work is licensed under a Creative Commons Attribution 4.0 International License.
Read Full License

Additional Declarations: No competing interests reported.

A Computational Framework for Predicting the Mechanical Properties of Recycled CFRP Laminates

Ilektra Tourkantoni[1] and Konstantinos Tserpes[2]

Laboratory of Technology and Strength of Materials, Department of Mechanical Engineering and Aeronautics, University of Patras, GR26504 Patras, Greece

[1]ORCID ID: 0009-0003-2815-8109

[2]ORCID ID: , Corresponding e-mail: kitserpes@upatras.gr

Abstract

The qualification of recycled carbon fiber reinforced polymers (CFRPs) requires reliable methodologies capable of linking constituent-level properties with laminate-scale mechanical performance. This work presents a multiscale property-transfer framework for predicting the behavior of unidirectional CFRP laminates manufactured using recycled carbon fibers recovered through a plasma-assisted solvolysis process. Single-fiber tensile and microbond tests were conducted to characterize the tensile and interfacial properties of virgin and recycled TR30S carbon fibers. The experimentally measured constituent properties were used as input to analytical micromechanical models for the prediction of the elastic constants and strength properties of a unidirectional ply. In addition, a 3D representative volume element was used to quantify the effect of interface degradation. The resulting ply properties were implemented in laminate-level finite element models and validated against experimental tensile, compression and interlaminar shear strength (ILSS) tests performed on both virgin and recycled CFRP laminates. Sensitivity studies evaluated the influence of fiber-strength and interface-strength degradation on the laminate response. Recycling reduced laminate tensile and compressive strength by less than 20%, while the ILSS decreased by 58%. The experimental tensile and compressive strengths lay within the numerical scatter band, and with an inter-ply tiebreak interface, the ILSS of the virgin laminates was predicted within 8%, whereas that of the recycled laminates was overpredicted owing to pre-existing damage. The results demonstrate that the proposed framework successfully transfers constituent-level degradation effects to the laminate scale and provides an efficient tool for predicting the mechanical performance of recycled composite structures.

Keywords: Plasma-assisted solvolysis; CFRP remanufacturing; Micromechanical analysis; Multi-scale modelling; Finite element analysis

1. Introduction

Recycled carbon fibers are increasingly considered a viable alternative to virgin fibers for the manufacturing of structural composite components [1–4]. Although recycling processes can preserve a large fraction of the original fiber stiffness, reductions in tensile strength and interfacial properties may affect the mechanical performance of the final composite [5, 6]. Experimental studies on composites remanufactured from recycled fibers have reported property losses of about 7–33% across several mechanical tests [7] and of about 36% in tensile strength [8], attributed mainly to degraded fiber–matrix adhesion after sizing loss. Consequently, reliable methodologies capable of transferring experimentally measured constituent properties to the structural scale are required to assess the suitability of recycled fibers for engineering applications [9, 10].

Several analytical and micromechanical approaches have been proposed in the literature for predicting the effective properties and strength of unidirectional composite plies. Classical formulations based on the mechanics of composite materials and the rule of mixtures provide the theoretical foundation for estimating laminate elastic constants and failure properties from constituent-level parameters. Daniel and Ishai [11] developed a comprehensive framework for linking constituent behavior with ply-level mechanical response, while Jones [12] presented analytical relationships for the prediction of elastic and strength properties of composite laminates. More recently, Vignoli et al. [13] proposed micromechanical formulations for the prediction of longitudinal and shear strengths of composite laminae, incorporating matrix and fiber interaction effects. Fiedler et al. [14] investigated the influence of thermal residual stresses on the transverse tensile strength of CFRPs through finite element analyses, highlighting the importance of local stress concentrations. Similarly, Bu et al. [15] demonstrated the strong dependence of transverse tensile strength on both matrix and interfacial properties, whereas Karkkainen and Martinez [16] evaluated a series of analytical approaches for the prediction of ply strengths in continuous carbon-fiber composites. However, these approaches have rarely been applied to recycled carbon fibers. Rouhi et al. [17] assessed micromechanical models for composites reinforced with recycled short carbon fibers and found that strength was degraded more than stiffness, with model predictions deviating more from the experiments for strength than for stiffness. Similarly, Sales-Contini et al.

[8] used the rule of mixtures for laminates made of pyrolysis-recycled fibers and reported large deviations from the measured moduli, attributed mainly to voids.

In parallel with micromechanical property prediction, finite element modelling has become a widely adopted tool for assessing the structural response and damage evolution of composite laminates. Progressive damage material models implemented in commercial explicit solvers allow the simulation of stiffness degradation and failure initiation under different loading conditions. Brown et al. [18] presented the formulation and capabilities of MAT_162 in LS-DYNA for modelling damage initiation and progressive failure in composite materials. Furthermore, combined experimental and numerical studies have demonstrated the capability of finite element models to accurately reproduce interlaminar shear behavior and predict failure mechanisms under short-beam loading conditions [19, 20]. Tan et al. [21] combined a micromechanical representative volume element, which predicted ply properties, with a mesoscale damage model of short-beam bending to show how fiber–matrix and interlaminar interface properties control the intralaminar and interlaminar damage of unidirectional laminates.

For recycled carbon fibers, finite element studies are scarcer. Gopalraj and Kärki [22] simulated the tensile and impact behavior of unidirectional recycled carbon and glass fiber epoxy composites in Abaqus using models calibrated on composite-level experimental data, without recycled fiber properties as input, and assuming defect-free material. Shi et al. [23] developed a numerical model of the influence of the arrangement and overlap of recycled discontinuous fibers on the strength of unidirectional composites. Recent reviews also note that studies comparing experimental and simulated data for recycled CFRPs remain limited [24].

Although the above studies have significantly advanced the understanding of ply-level property prediction, studies on recycled carbon fibers are mostly experimental or calibrated at the composite level [7, 8, 17, 22, 23], whereas multiscale models linking fiber and interface properties to laminate response mainly address virgin fibers [21]. In contrast, limited work has focused on directly transferring experimentally measured properties of recycled carbon fibers, such as fiber strength and interfacial shear strength, to laminate-scale numerical simulations and validating the predictions against multiple laminate loading configurations. To address this research gap, the present work develops and validates a multiscale property-transfer route for carbon fiber reinforced polymer laminates manufactured with recycled carbon fibers.

2. Computational Framework

The methodology is illustrated in Fig. 1, showing the overall computational framework. The proposed computational framework adopts a multiscale approach to predict the mechanical properties of recycled CFRP laminates, integrating constituent, ply, and laminate levels. At the constituent level, experimental inputs include matrix and fiber properties, fiber/matrix interfacial strength, and fiber volume fraction. Two complementary modelling approaches are employed to determine the mechanical properties of unidirectional (UD) plies. Model A uses analytical micromechanical formulations, including Mori–Tanaka, improved Halpin–Tsai, Chamis, and bridging models. Model B employs a representative volume element (RVE)-based finite element approach to explicitly represent the composite microstructure. The RVE model incorporates cohesive fiber/matrix interfaces, periodic boundary conditions, and finite element homogenization. Both approaches predict the elastic moduli and strengths of UD plies, providing the inputs for subsequent laminate-level analysis. At the laminate level, the predicted ply properties are used to determine the tensile, compressive, and interlaminar shear strength (ILSS) properties of recycled CFRP laminates. The numerical predictions are validated against experimental tensile, compression, and ILSS test results. The framework enables the assessment of the predictive capabilities of analytical and numerical micromechanical approaches for recycled CFRP laminates and can be extended to structural parts such as composite stiffened panels.

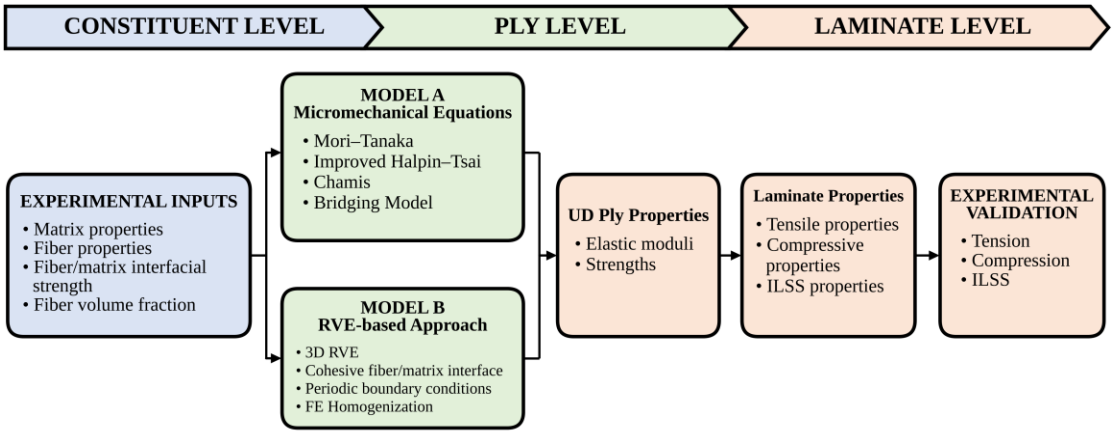

Fig. 1 Flowchart of the computational framework.

3. Experimental input

3.1 Fiber-Level Characterization

The recycled carbon fibers were recovered through a solvolysis-based recycling process. The recycling parameters included a power input of 1200 W, nitric acid concentration of 14.4 M, treatment duration of 6 h, plasma gas ratio O_2/Ar = 1/4 and an initial composite mass of 32.8 g. A detailed description of the plasma-assisted solvolysis process is provided in our previous work [25].

Single-fiber tension tests were performed to determine the tensile strength, elastic modulus and failure strain of both virgin and recycled carbon fibers, using a tensile testing machine equipped with 5 N load cell (X100-1LT, Testometric Ltd., Rochdale, UK) in accordance with ASTM C1557–14 [26]. In addition, microbond testing was conducted to evaluate the fiber–matrix interfacial shear strength (IFSS) [27], which was subsequently used in the analytical prediction of matrix-dominated ply strengths. Data were collected at a sampling frequency of 50 Hz using a FIBRObond microdroplet tester (Fibrobotics, Tampere, Finland). The experimental setups employed for the fiber-level characterization are shown in Fig. 2.

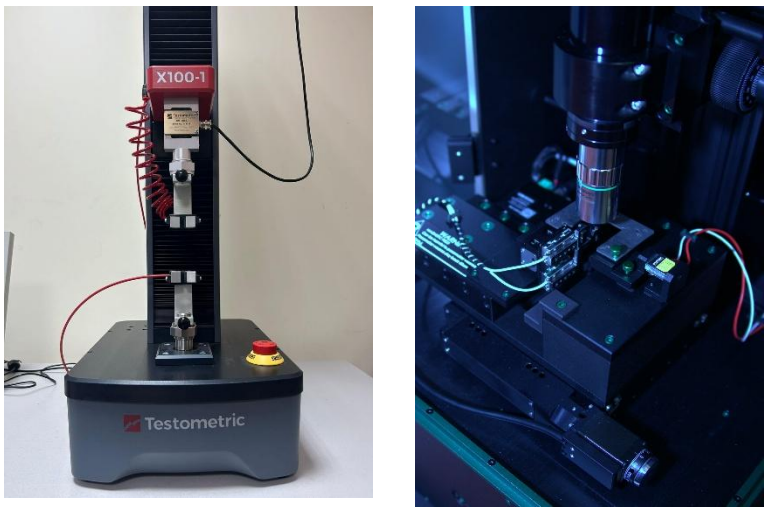

(a) (b)

Fig. 2 Experimental setups for fiber characterization: (a) single-fiber tensile testing and (b) microbond testing.

The experimental results indicated that the recycled fibers retained their stiffness and tensile strength after recycling. The average tensile strength increased from 2217.75 ±721.35 MPa for the virgin fibers to 2299.55±1129.28 MPa for the recycled fibers, while the elastic modulus increased from 211.19±11.43 GPa to 221.14±11.49 GPa. In contrast, the interfacial shear strength decreased from 51.67±7.79 MPa to 40.54±7.47 MPa, indicating a deterioration of the fiber–matrix interface after recycling. The remaining input parameters required by the analytical models were obtained

from the literature and appropriately scaled for the recycled fibers [28]. Table 1 summarizes the material properties adopted for the fibers and Table 2 the matrix properties, which were mainly taken from the manufacturer's datasheet. $E_{1,f}$, $E_{2,f}$, $E_{3,f}$ are moduli of the fiber; $\nu_{12,f}$, $\nu_{23,f}$ are fiber Poisson's ratios; $G_{12,f}$, $G_{23,f}$ are fiber shear moduli; E_m, ν_m, G_m are matrix modulus, Poisson's ratio and shear modulus and $S_{u,m}$, $\varepsilon_{ut,m}$ are matrix tensile strength and failure strain.

Table 1 Mechanical properties of the virgin and recycled TR30S carbon fibers.

Property	Units	Virgin fibers	Recycled fibers
$E_{1,f}$	GPa	211.19	221.14
$E_{2,f}$, $E_{3,f}$	GPa	15	15.71
$\nu_{12,f}$	-	0.29	0.3037
$\nu_{23,f}$	-	0.07	0.0733
$G_{12,f}$	GPa	15	15.71
$G_{23,f}$	GPa	7	7.33

Table 2 Mechanical properties of the epoxy matrix.

Property	Units	Matrix
E_m	GPa	3.4
$\varepsilon_{ut,m}$	%	5.1
$S_{u,m}$	MPa	90
ν_m	-	0.33
G_m	GPa	1.28

3.2 Laminate-Level Characterization

The laminate-level experimental campaign was performed on CFRP laminates manufactured using both virgin and recycled TR30S carbon fibers. The recycled fibers originated from filament-wound composite cylinders produced by B&T Composites (Florina, Greece). The remanufactured laminates were fabricated in-house using a hand lay-up process, followed by vacuum bagging and curing, resulting in a six-ply UD laminate configuration.

The recycled CFRP cylinders consisted of TR30S carbon fibers embedded in an anhydride-cured epoxy system based on EPIKOTE™ 828 resin and EPIKURE™ 866 hardener. New laminates were manufactured using the same reinforcement and a two-part epoxy system (SR1700/SD2803, Sicomin, France). Prepregs were produced through a hand lay-up process by impregnating aligned carbon-fiber tows with the epoxy resin. The layups were vacuum-bagged, cured for 24 h at room temperature under 2 bar pressure and post-cured at 60°C for 16 h. Optical microscopy measurements indicated an average fiber volume fraction of approximately 57% [29].

Experimental characterization was performed under three loading configurations. Tensile tests were conducted according to ASTM D3039 [30] using a universal testing machine equipped with an extensometer to determine the longitudinal tensile modulus, tensile strength and failure strain of the laminates. Compression tests followed ASTM D3410 [31] to evaluate the compressive stiffness and strength. Interlaminar shear behavior was assessed through short-beam testing according to ASTM D2344 [32] using a three-point bending fixture, providing the interlaminar shear strength (ILSS). The experimental setups for the three laminate-level tests are shown in Fig. 3.



(a) (b) (c)

Fig. 3 Experimental setups for laminate characterization: (a) tensile testing; (b) compression testing; and (c) interlaminar shear strength testing [29].

The experimental results revealed that the recycled laminates retained stiffness levels comparable to those of the virgin material, exhibiting tensile moduli of 175.07 GPa and 180.95 GPa, respectively. In contrast, strength-related properties were more strongly affected by recycling. The tensile strength decreased from 1538.55 MPa for the virgin laminates to 1236.43 MPa for the recycled laminates, while the compressive strength decreased from 593.48 MPa to 513.41 MPa. The most significant reduction was observed in the interlaminar shear response, where the ILSS decreased from approximately 66 MPa for the virgin laminates to approximately 28 MPa for the recycled laminates. This behavior is consistent with the reduction in interfacial shear strength measured during the microbond tests and highlights the dominant role of the fiber–matrix interface in shear-dominated loading conditions. Similarly, the removal of the sizing agent during solvolysis recycling changes the interfacial bonding between recycled fibers and fresh resin, affecting the performance of the remanufactured composites [33]. The condition of the recycled

fiber surface, in particular the presence of residual resin, has also been shown to affect the strength of the resulting composites [34], while the influence of interfacial properties on the interlaminar damage of UD laminates has been demonstrated through experiments and multiscale modelling [21].

4. Analytical Computation of Ply Properties

4.1 Elastic Constants

Four micromechanical models were employed to predict the effective elastic properties of UD CFRP plies: Mori–Tanaka, Bridging, improved Halpin–Tsai, and Chamis. The Mori–Tanaka model [35] treats the composite as a two-phase material consisting of transversely isotropic fibers embedded in an isotropic matrix. Based on the elastic properties and volume fractions of the constituents, the model estimates the effective orthotropic elastic properties of the UD ply. The Bridging model [36] accounts for the mechanical interactions between the fibers and matrix through a bridging formulation. In the three-phase implementation adopted here, the composite is represented by the fibers, matrix, and interphase. The homogenization procedure involves two successive steps: first, the fibers and interphase are combined into an equivalent two-phase subsystem; subsequently, this subsystem is combined with the matrix to determine the effective composite response. The formulation can also account for matrix elastoplasticity and the resulting nonlinear composite response. The improved Halpin–Tsai model [37] extends the conventional two-phase formulation by explicitly incorporating the influence of the fiber–matrix interphase on the effective elastic properties. The composite is represented as a three-phase system consisting of fibers, matrix, and interphase. The homogenization is performed through two sequential two-phase models. First, the fibers and surrounding interphase are combined into an equivalent reinforcement phase. This equivalent phase is then embedded in the matrix to determine the effective properties of the composite. The fibers are assumed to be transversely isotropic and uniformly distributed, whereas the matrix and interphase are considered isotropic and defect-free. The Chamis model [38] employs simplified micromechanical relationships based on the rule of mixtures and constituent-level properties to estimate the effective elastic constants of the UD ply. The longitudinal elastic modulus is primarily governed by the fiber properties and volume fraction, whereas the transverse elastic modulus and shear moduli are more strongly influenced by the

matrix properties. The model assumes linear elastic constituent behavior and provides a computationally efficient approach for estimating the effective ply properties.

The complete set of equations for all four models are depicted in Appendix A. Among the four models, Mori–Tanaka was adopted for the laminate-level simulations, as its predicted longitudinal and transverse stiffness were within about 8% of the RVE reference.

4.2 Strengths

When the composite is subjected to longitudinal tension, the load is primarily carried by the fibers, while the matrix transfers stress between them [16, 39–41]. Assuming perfect fiber–matrix bonding and uniform stress distribution, the longitudinal tensile strength of the ply can be expressed through the Rule of Mixtures:

$$S_1^t = S_{u,f}\left(\mathrm{V_f} + \mathrm{V}_m\ \frac{E_m}{E_{1,f}}\right), \tag{1}$$

where $S_{u,f}$ is the ultimate strength of the fiber and $\mathrm{V_f}$, V_m are the fiber and matrix volume fraction, respectively.

This equation assumes that all fibers experience the same strain and fail simultaneously. In practice, fiber failure occurs progressively due to the statistical variation of fiber strength. Local matrix shear stress near broken fibers redistributes the load to neighboring intact fibers until the accumulation of fiber breaks and interfacial debonding leads to catastrophic failure. Thus, Eq. (1) provides an upper-bound estimation for the composite tensile strength, with deviations depending on the fiber–matrix adhesion quality and fiber alignment.

The transverse tensile strength is governed almost entirely by the matrix, since the fibers offer minimal reinforcement in the transverse direction [39]. The stress transfer and local concentration near the fiber–matrix interface strongly influence failure. To predict this strength, the Bridging model is applied while considering stress concentration effects within the matrix. The transverse tensile strength of the ply can be written as:

$$S_2^t = \min\left\{\left(\left(V_f + \beta\ V_m\right) E_{2,f} + (1-\beta)\ V_m\ E_m\right)\frac{S_{u,f}}{E_{2,f}}, \left(\left(V_f + \beta\ V_m\right)E_{2,f} + (1-\beta)\ V_m\ E_m\right)\frac{S_{u,m}}{(\beta E_{2,f} + (1-\beta)E_m)\ K_{22}^t}\right\}, \tag{2}$$

where β is the bridging parameter of the Bridging model and K_{22}^t is the transverse stress concentration factor:

$$K_{22}^{t} = \left(1 + \frac{V_f^{0.5}}{2} A + \frac{V_f^{0.5}}{2}\left(3 - V_f - V_f^{0.5}\right) B\right) \frac{\left(V_f + V_m\,\beta\right) E_{2,f} + V_m\,(1-\beta)\,E_m}{\beta E_{2,f} + (1-\beta) E_m}, \quad (3)$$

where A and B are functions of the Poisson ratios (ν_f^{23}, ν_m) and the elastic moduli, representing the mismatch in transverse deformation between the fiber and matrix. Failure occurs when the maximum principal stress in the matrix reaches its tensile strength, consistent with the Maximum Stress Criterion.

Under longitudinal compression, the composite may fail by fiber micro-buckling, kinking, or fiber fracture. The onset of these failure modes is often triggered by small imperfections such as fiber misalignment or waviness, combined with matrix plasticity. Since micro-buckling and kinking dominate the behavior under compression, the longitudinal compressive strength is lower than the tensile strength [16]. An empirical factor is applied to approximate this reduction:

$$S_1^c = 0.69 \times 0.78 V_f\, S_{u,f}, \quad (4)$$

where 0.78 is an empirical efficiency factor of the fiber tensile strength [16]. This reduction accounts for fiber anisotropy, nonlinear shear in the matrix, and imperfect alignment. The factor is derived from experimental comparisons across multiple CFRP systems and has been shown to give accurate estimates of compressive strength at the ply level.

Transverse compression introduces high localized stresses at the fiber–matrix interface, potentially leading to matrix yielding, shear cracking, or fiber crushing [11]. The predicted transverse compressive strength is given by:

$$S_2^c = \frac{S_{c,m} + \sigma_{rm}}{k_\sigma}, \quad (5)$$

where $S_{c,m}$ is the matrix compressive strength, σ_{rm} is the residual radial stress at the interface, and k_σ is the stress concentration factor:

$$k_\sigma = \frac{1 - V_f\left(1 - \frac{E_m}{E_{1,f}}\right)}{1 - \left(4\,\frac{V_f}{\pi}\right)^{0.5}\left(1 - \frac{E_m}{E_{1,f}}\right)} \quad (6)$$

This approach models the composite as a heterogeneous assembly of fibers within a matrix, arranged in a square pattern, and provides a realistic estimate of the onset of local matrix crushing or interfacial failure.

When a shear load is applied in the 1–2 plane, the composite exhibits a nonlinear stress–strain response due to matrix cracking and interfacial slip. Different definitions of shear strength

exist—onset, yield, and rupture shear strength—depending on the stage of damage [13]. The in-plane shear strength is predicted using a combination of the Bridging model and a stress concentration correction:

$$S_{12}^{s} = \frac{S_{s,m}}{K_{12}\, L_4}, \tag{7}$$

where $S_{s,m}$ is the matrix shear strength and K_{12} and L_4 are defined as:

$$K_{12} = \left(1 - V_f \left(\frac{G_{12,f} - G_m}{G_{12,f} + G_m}\right)\left(W - \frac{1}{3}\right)\right)\left(\frac{V_f + \alpha_{66}\left(1 - V_f\right)}{\alpha_{66}}\right) \tag{8}$$

$$W = \pi\, V_f^{0.5}\left(\frac{1}{4\, V_f} - \frac{4}{128} - \left(\frac{2}{152}\right) V_f - \left(\frac{5}{4096}\right) V_f^2\right) \tag{9}$$

$$L_4 = \frac{\alpha_{66}}{\left(V_f + \alpha_{66}\right)\left(1 - V_f\right)} \tag{10}$$

$$\alpha_{66} = 0.3 + 0.7\left(\frac{G_m}{G_{12,f}}\right) \tag{11}$$

5. RVE Finite Element (FE) modelling

To investigate the influence of the fiber–matrix interface on the mechanical response of the CFRP composite, a three-dimensional hexagonal RVE was developed to accurately represent the microstructure of a unidirectional composite ply. The model consisted of cylindrical carbon fibers embedded within an epoxy matrix and was designed to achieve the target fiber volume fraction (Fig. 4). Periodic Boundary Conditions (PBCs) were applied to ensure a representative response and to minimize edge effects [42]. The dimensions of the RVE were: $L_x = 4.42$ μm, $L_y = 8.83$ μm, $L_z = 15.29$ μm [43].

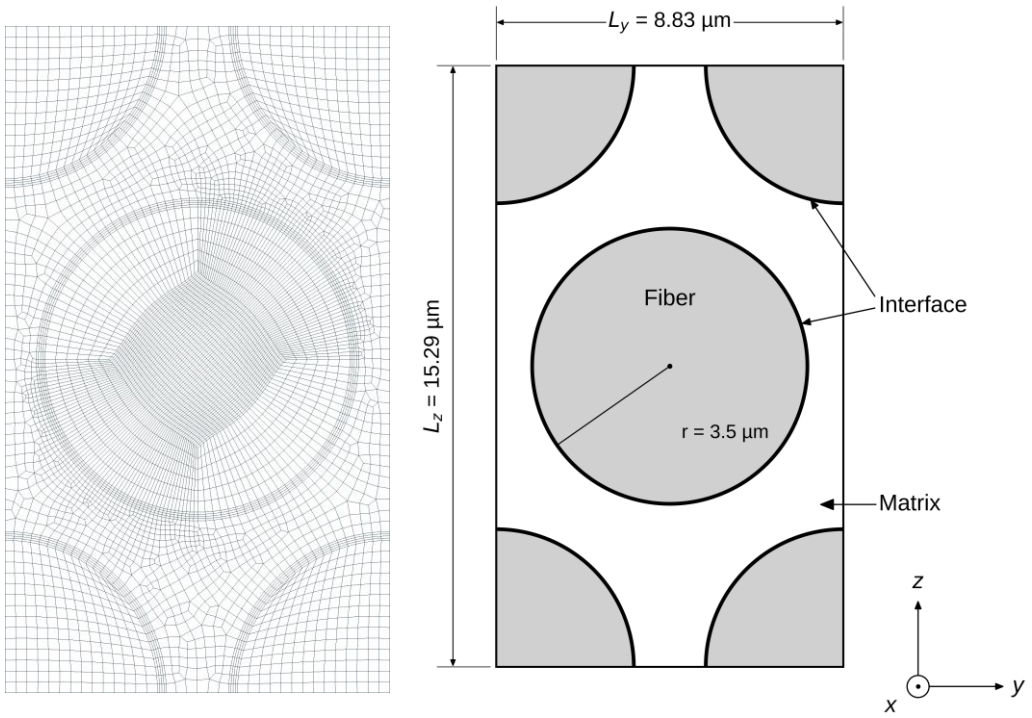

(a) (b)

Fig. 4 Cross-section of the RVE model: (a) finite element mesh and (b) geometry.

The fiber–matrix interface was modelled using a bilinear cohesive model with zero thickness. The contact remains bonded until a critical traction-based failure criterion is reached, after which debonding and separation are allowed. The interface properties were defined using the experimental value of IFSS as the shear failure strength and the normal interface strength was defined as [44]:

$$\sigma_n = \frac{2}{3}\tau_{IFSS}, \tag{12}$$

where σ_n and τ_{IFSS} are the normal and shear strength of the interface. The fibers were modelled as a linear elastic material, and the matrix behavior was represented using a polymer plasticity material model capable of capturing nonlinear deformation prior to failure. In addition, fiber and matrix failure were modelled using a maximum stress criterion. Element deletion occurred once the maximum principal stress exceeded the prescribed fiber strength.

6. Laminate FE Modelling

Finite element simulations were performed in LS-DYNA to reproduce the experimental tension, compression and interlaminar shear tests and to evaluate the predictive capability of the proposed

multiscale methodology. The analytically predicted ply properties were directly implemented at the laminate level and used as input for all numerical models. Fig. 5 shows the FE mesh of the ILSS model. The coupon dimensions (length × width × thickness) were 138 × 15 × 1 mm for the tension tests, 15 × 15 × 1 mm for the compression tests and 18 × 6 × 3 mm for the ILSS tests, in accordance with the test standards described in Section 3.2. In the ILSS configuration, the loading nose and the two supports were modelled as cylinders with diameters of 6 mm and 3 mm, respectively. The composite laminates were modelled using a composite damage model, which enables the simulation of progressive damage initiation and stiffness degradation in unidirectional fiber-reinforced composites. The material model accounts for the major intralaminar failure mechanisms, including fiber tensile failure, fiber compressive failure, matrix cracking and matrix crushing, through a Hashin-type damage formulation. Delamination capabilities available within the material model were also activated to account for interlaminar damage evolution [45].

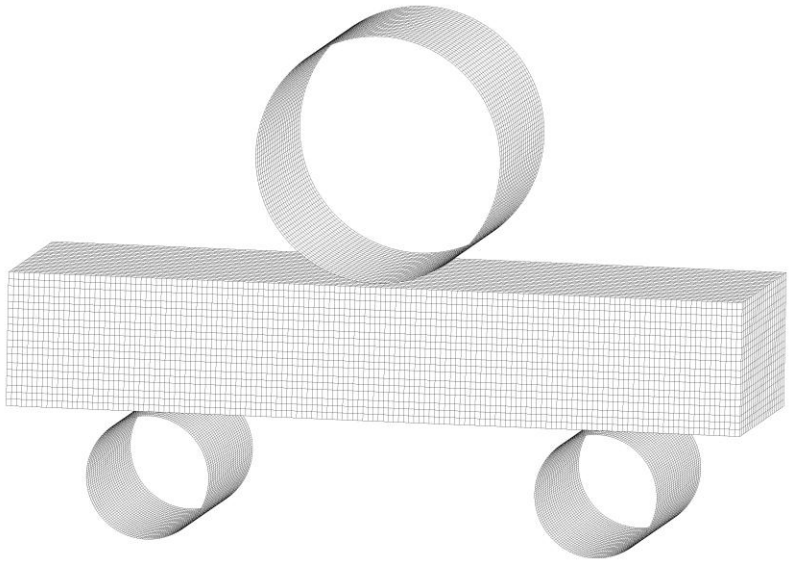

Fig. 5 Typical FE mesh of the ILSS coupon and the supporting and loading cylinders.

Three FE models were developed, corresponding to the experimental tensile, compression and short-beam shear standard tests. All laminates consisted of six unidirectional plies with a fiber orientation of 0°. The laminate plies were discretized using fully integrated 3D solid elements. Three solid elements were assigned through the thickness of each ply to ensure an accurate representation of the through-thickness stress distribution while maintaining computational efficiency. The short-beam shear model included rigid cylindrical supports and a loading nose, reproducing the experimental fixture used during the tests; to reduce the computational time and

cost, these cylinders were meshed with shell elements. Mesh densities were selected following convergence studies to achieve mesh-independent predictions of the structural response.

For the tension and compression simulations, displacement-controlled loading was applied to reproduce the experimental boundary conditions and ensure predominantly uniaxial loading. Contact interactions between the laminate and the loading fixtures were defined using surface-to-surface contact formulations.

To account for the interlaminar defects observed in the recycled laminates through C-scan inspection, the interfaces between adjacent plies were additionally represented using a tiebreak contact formulation. This approach enables the initiation and propagation of delamination through a traction–separation law once the interfacial strength is exceeded [19].

7. Results and Validation

7.1 Recycled Ply Properties

The analytically predicted elastic properties of UD plies reinforced with virgin and recycled carbon fibers are presented in Tables 3 and 4, respectively. All micromechanical models yield comparable predictions, except for the Bridging model, which provides estimates approximately 10% higher than those obtained using the other approaches. Furthermore, all models predict slightly higher elastic constants for the recycled-fiber composites, with the most pronounced increase observed in the longitudinal elastic modulus. This increase is attributed to the higher elastic modulus measured for the recycled fibers during the single-fiber tension tests. E_1 is the longitudinal modulus of the composite ply, E_2 the transverse and G_{12} the shear modulus, and ν_{12} is the in-plane Poisson's ratio.

Table 3 Predicted elastic constants of the UD plies with virgin fibers.

Model	E_1 [GPa]	E_2 [GPa]	G_{12} [GPa]	ν_{12}
Mori-Tanaka Model	117.68	7.48	3.49	0.307
Bridging Model	127.02	12.58	4.63	0.339
Halpin Tsai Model	119.97	16.04	4.82	0.325
Chamis Model	117.68	7.41	2.57	0.308

Table 4 Predicted elastic constants of the UD plies with recycled fibers.

Model	E_1 [GPa]	E_2 [GPa]	G_{12} [GPa]	ν_{12}
Mori-Tanaka Model	123.16	7.60	3.52	0.315
Bridging Model	132.93	12.78	4.71	0.347
Halpin Tsai Model	125.54	16.23	4.91	0.333

Chamis Model	123.16	7.42	2.58	0.316

For the sake of comparison, the effective elastic properties were also computed using the RVE-based FE model. Homogenization was achieved using periodic boundary conditions under a small, applied strain of 0.1%, assuming undamaged material behavior. The RVE was discretized using 3D Tet4 elements. Implicit FE analyses were performed using linear elastic constituent models. The resulting elastic constants are $E_1 = 126.23$ GPa, $E_2 = 6.96$ GPa and $G_{12} = 4.54$ GPa, respectively, which are very close to the analytical values.

The analytically predicted ply strengths are compared in Fig. 6. The longitudinal tensile and compressive strengths increased from 1279.47 MPa to 1325.95 MPa and from 680.83 MPa to 705.44 MPa, respectively. These improvements are consistent with the experimental results, which showed that the recycled fibers retained and slightly improved their tensile strength and elastic modulus. Since the longitudinal response of a unidirectional composite is primarily governed by the fibers, the enhanced fiber properties are reflected in the corresponding ply strengths. In contrast, the transverse and shear strengths remained nearly unchanged. These properties are mainly controlled by the matrix and the fiber–matrix interface and are therefore less sensitive to the changes in the fiber properties. Although the microbond tests indicated a reduction in interfacial shear strength after recycling, this effect is not explicitly considered in the analytical models, which assume perfect bonding between the fibers and the matrix.

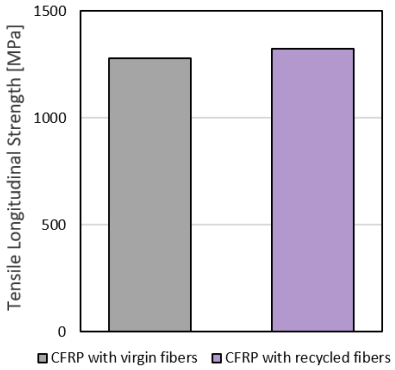

(a)

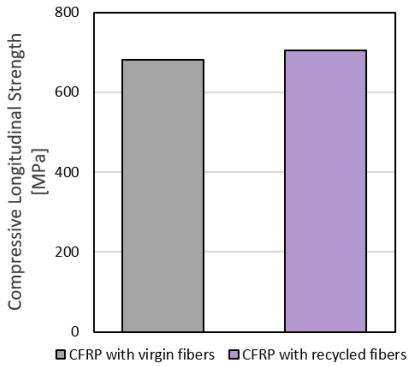

(b)

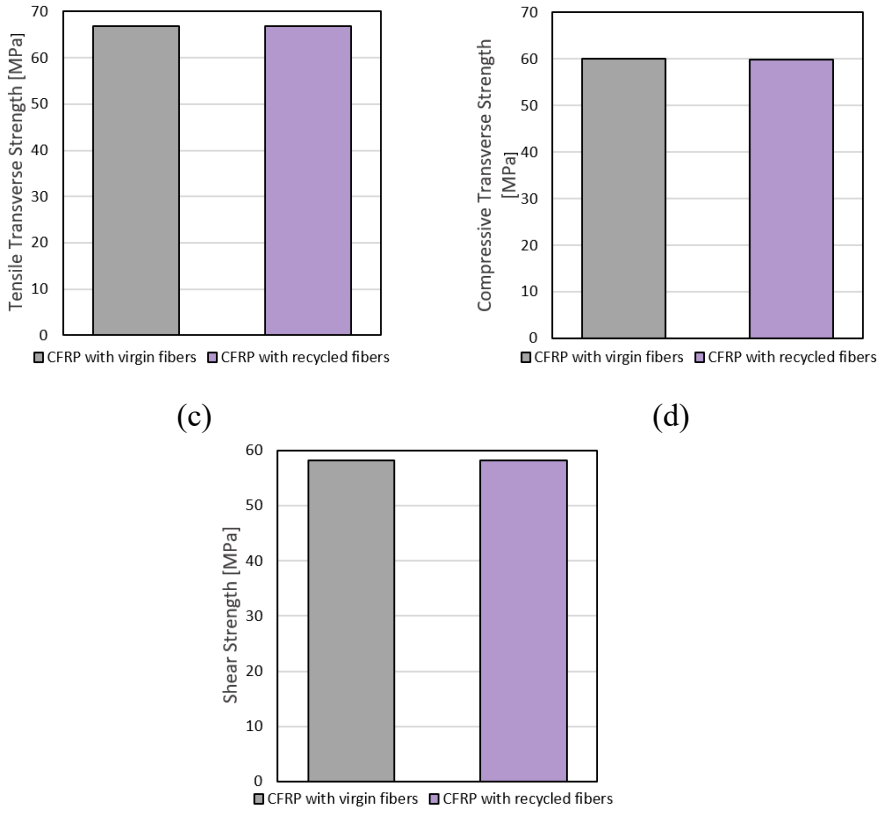

Fig. 6 Predicted strength properties of virgin and recycled CFRP plies: (a) longitudinal tensile strength; (b) longitudinal compressive strength; (c) transverse tensile strength; (d) transverse compressive strength; and (e) in-plane shear strength.

7.2 Sensitivity Analyses of Fiber Strength and Interfacial Strength

To investigate the sensitivity of laminate performance to reductions in fiber strength, additional analyses were conducted by considering reductions of 6%, 12%, and 24% in the longitudinal tensile and compressive strengths of the fibers relative to their experimentally measured values. Table 5 summarizes the corresponding longitudinal ply strengths predicted using Equations (1) and (3) for each degradation scenario. Owing to the linear dependence of the predicted ply strengths on the corresponding fiber strengths, the reductions in ply strength were proportional to those imposed on the fibers.

Table 5 Fiber-strength degradation scenarios considered in the sensitivity study.

Degradation	S_1^t **[MPa]**	S_1^c **[MPa]**
0%	1279.47	680.83
6%	1202.70	639.98

12%	1125.93	599.13
24%	972.40	517.43

The computed ply strengths listed in Table 5 were subsequently implemented in the laminate simulations. The tensile response (Fig. 7a) exhibits a more gradual dependence on fiber strength degradation. Small reductions in fiber strength produce limited changes in laminate tensile strength, while larger degradations lead to progressively higher reductions. The compressive strength (Fig. 7b) does not decrease linearly with the degradation of the virgin fiber strength. A 6% reduction in fiber strength results in a large reduction in laminate compressive strength. Further degradation leads to additional strength losses, although at a progressively lower rate. The ILSS results (Fig. 7c) revealed a significant reduction in interlaminar performance after degradation. Fig. 7c shows that the maximum load decreased from 2280.5 N for the virgin laminates to 1916.6 N, 1856.7 N, and 1855.5 N for the 6%, 12%, and 24% degradation levels, respectively. This corresponds to an overall reduction of approximately 19% compared to the virgin material. Most of the reduction occurred between the virgin and 6% degradation conditions, while only minor changes were observed at higher degradation levels. This behavior suggests that the initial stages of degradation have the greatest impact on the fiber–matrix interface, which governs the interlaminar shear response. The trend is consistent with the microbond test results, which showed a decrease in interfacial shear strength after recycling.

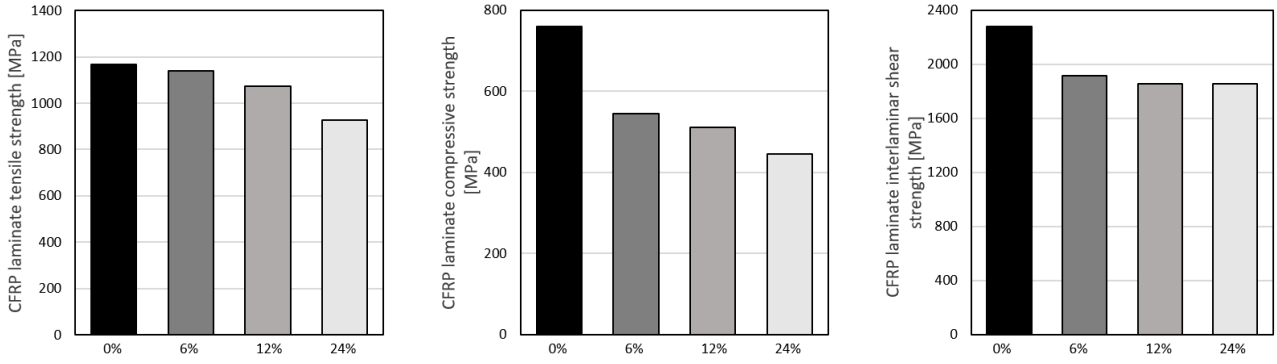

(a) (b) (c)

Fig. 7 Response of CFRP laminates for different fiber-strength degradation scenarios for (a) tension tests; (b) compression tests; and (c) ILSS tests.

To establish a reference point for the subsequent sensitivity analysis, the ply response was first evaluated under two different interface assumptions. The developed RVE-based interface model was compared against an idealized perfect bonding condition, where complete load transfer

between the fiber and matrix was assumed. The obtained ply strengths for both cases are presented in Fig. 8.

The comparison between the cohesive interface model and the perfect bonding assumption highlights the significant role of the interface in controlling the transverse and shear-dominated strength properties of the UD ply. While the longitudinal tensile and compressive strengths remain relatively insensitive to the interface representation, with reductions of approximately 6% and less than 1%, respectively, larger differences are observed for the transverse and shear strengths. The most pronounced effect is observed in the shear response, where the predicted strengths decrease by approximately 30–50%. This indicates that the fiber–matrix interface primarily governs load transfer under shear loading conditions, whereas longitudinal strength remains mainly controlled by the fiber properties.

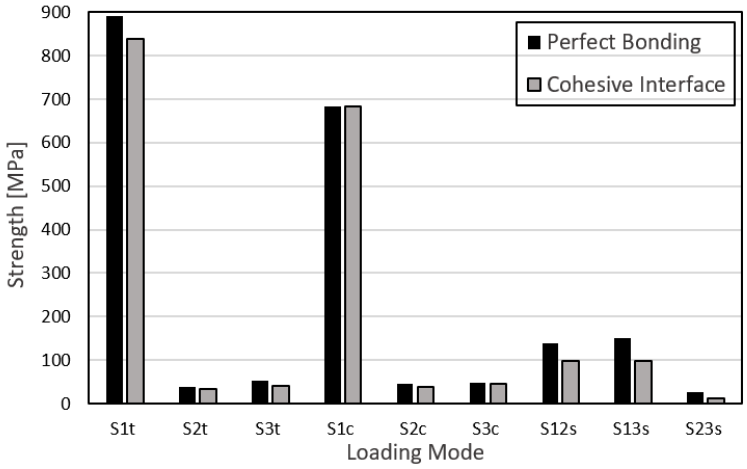

Fig. 8 Comparison of predicted virgin UD ply strength properties obtained using the cohesive interface model and the perfect bonding assumption.

To investigate the sensitivity of laminate performance to reductions in interface strength, additional simulations were performed by artificially degrading the longitudinal normal and shear strength of the interface by 12%, 24% and 48% relative to the experimentally measured value derived from microbond experiments (Table 6). The percentages of degradation of the interface's strength were chosen larger than those for the fiber strength because the literature reports that solvolysis degrades the interface more readily than the fibers [25, 46].

Table 6 Interface-strength degradation scenarios considered in the sensitivity study.

Degradation	Shear Strength [MPa]	Normal Strength [MPa]

0%	51.67	34.45
12%	45.47	30.31
24%	39.27	26.18
48%	26.87	17.91

The most interesting results are observed under transverse loading, where the mechanical response is primarily governed by the matrix and the fiber–matrix interface. The predicted transverse tensile strength decreased by 0.99%, 8.25%, and 19.63% for the considered degradation scenarios, exhibiting an almost proportional relationship with the imposed interface degradation. In contrast, the reduction in transverse compressive strength was smaller and more gradual, reflecting the combined contribution of multiple failure mechanisms, including matrix yielding and local stress redistribution. Similar observations were reported by Wang et al. [47], who demonstrated that reductions in fiber–matrix interfacial properties lead to a nearly proportional decrease in transverse tensile strength. As shown in Fig. 9a, crack initiation occurs within the matrix, close to the central and right-side fibers. As the loading progresses, the damage propagates through the matrix regions located between the interfaces (Fig. 9b). Eventually, complete debonding between the fibers and the matrix is observed, accompanied by the deletion of several matrix elements due to severe damage accumulation (Fig. 9c).

In contrast, under longitudinal loading, the applied load is carried mainly by the fibers. Consequently, damage initiation and element deletion occur mainly within the fibers themselves, leading to fiber-dominated failure prior to significant matrix damage, as illustrated in Fig. 10.

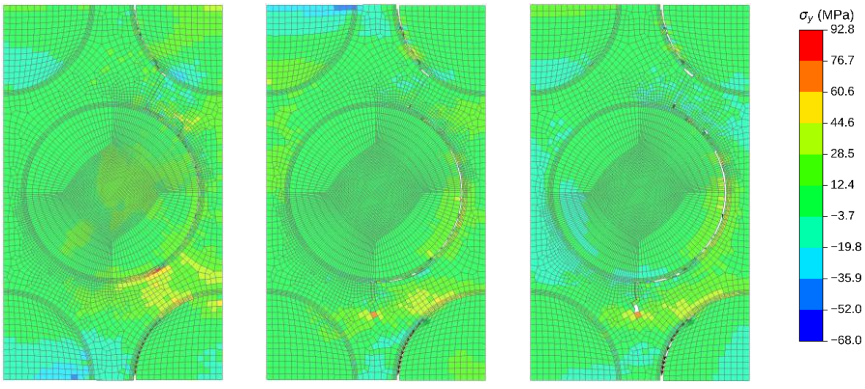

Fig. 9 Progressive damage evolution of the RVE under transverse tensile loading: (a) crack initiation within the matrix; (b) damage propagation through the matrix-rich regions; (c) complete fiber–matrix debonding and (d) the corresponding stress scale used to quantify local stress concentrations.

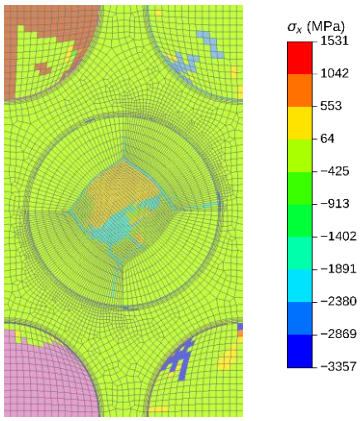

(a) (b)

Fig. 10 Contour plot of normal stress developed in the RVE model during longitudinal tensile loading: (a) stress distribution within the RVE and (b) the corresponding stress scale used to quantify local stress concentrations.

The homogenized strength properties obtained from the RVE analyses for each interface-degradation scenario were subsequently employed as input parameters for the laminate-level simulations. This multiscale framework enabled the propagation of microscale interface damage effects to the laminate scale, allowing the sensitivity of the laminate mechanical response to interface degradation to be systematically evaluated. Fig. 11 demonstrates that the influence of interface degradation strongly depends on the dominant load-transfer mechanism associated with each loading condition. The largest sensitivity is observed under longitudinal tensile loading, where even a moderate reduction in interface strength leads to a significant decrease in laminate strength. Although the longitudinal response of unidirectional laminates is primarily governed by the fibers, the interface remains responsible for transferring stresses between the matrix and the reinforcement and for maintaining strain compatibility. Consequently, interface weakening promotes earlier debonding and stress redistribution, resulting in premature fiber failure and a substantial reduction in tensile strength. A similar trend is observed for the ILSS response, where interlaminar performance is directly controlled by the ability of the interface to sustain shear stresses. The results indicate that most of the strength reduction occurs at the initial stages of degradation, while further decreases in interface properties produce only limited additional reductions, suggesting that a critical interfacial damage threshold is reached. In contrast, the compressive response exhibits a lower sensitivity to interface degradation.

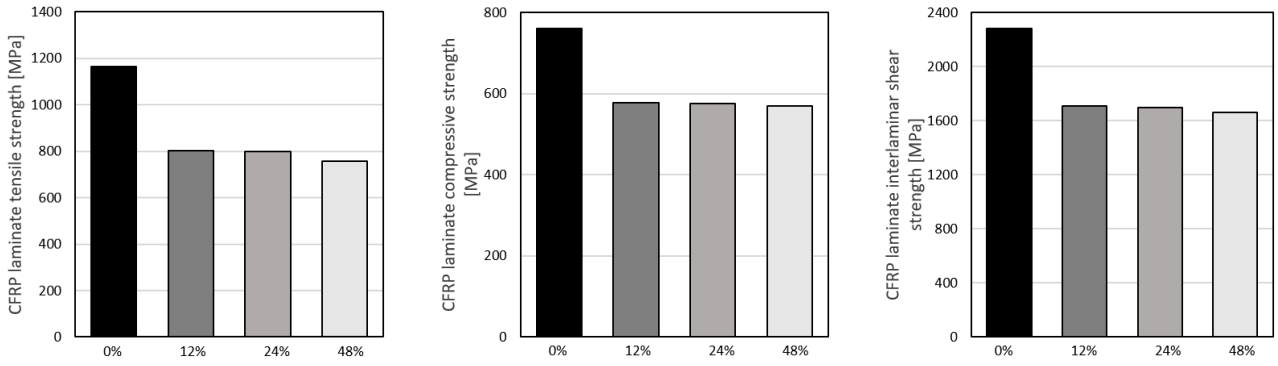

(a) (b) (c)

Fig. 11 Response of CFRP laminates for different interface-strength degradation scenarios for (a) tension tests; (b) compression tests; and (c) ILSS tests.

A comparison between the two sensitivity studies reveals distinct roles of fiber and interface degradation on laminate performance. Fiber-strength degradation strongly affects the compressive response, with a large initial reduction followed by smaller losses, while the tensile strength decreases more gradually. In contrast, interface degradation has a much stronger impact on tensile performance. Even though the longitudinal response of unidirectional laminates is generally considered fiber-dominated, the results demonstrate that the integrity of the fiber–matrix interface plays a critical role in ensuring efficient stress transfer and delaying the onset of local damage mechanisms. Moreover, the interlaminar shear strength exhibits a similar trend in both degradation studies, with a pronounced initial reduction followed by more moderate decreases, suggesting the existence of a threshold beyond which additional degradation has a limited influence on damage initiation.

The most pronounced effect is observed in the ILSS response, where reductions in interface strength led to significant decreases in both stiffness and maximum load-carrying capacity. Most of this reduction occurs during the initial degradation stages, while further decreases in interface properties result in comparatively smaller changes in the laminate response. This trend suggests the existence of a critical interfacial damage threshold beyond which the sensitivity of the structural response becomes less significant. Furthermore, the load fluctuations observed in the numerical curves are associated with the progressive damage formulation of the material model and correspond to successive debonding and stiffness-degradation events occurring during loading.

7.3 Validation of the Multiscale Methodology

The results presented in the previous sections revealed a noticeable discrepancy between the numerical and experimental responses obtained from the ILSS tests. Although the laminate stiffness and overall trends were captured satisfactorily, the simulations consistently overpredicted the maximum load-carrying capacity. This behavior was mainly attributed to the assumption of perfect bonding between adjacent plies, which prevented the initiation and propagation of interlaminar damage observed experimentally. To address this limitation, the laminate model was enhanced by a contact tiebreak between adjacent plies. The tiebreak formulation allows progressive degradation of the interlaminar bond and enables delamination initiation once the prescribed normal and shear strength limits are exceeded [48, 49]. The bilinear traction–separation law used from contact tiebreak type 9 enables the simulation of interlaminar damage initiation and propagation, resulting in an accurate prediction of the laminate stiffness and a significantly improved estimation of the maximum force. A slight overprediction of the peak load is still observed for the recycled laminates, possibly due to pre-existing damage that is not explicitly included in the model.

The multiscale methodology was validated through direct comparison between the analytical and numerical predictions and the experimental results obtained from the laminate tests. Fig. 12 presents the final validation results through the stress–strain curves for the three loading cases, comparing the two modelling approaches. Figs. 13 and 14 compare the predicted and measured mechanical properties of the CFRP laminates manufactured with virgin and recycled carbon fibers, respectively. The numerical predictions were generated by considering the experimental scatter of the fiber tensile strength through its measured standard deviation. For tensile loading, the simulations successfully reproduced the stiffness and strength of both virgin and recycled laminates and captured the reduction in strength associated with the recycled fibers. The remaining discrepancies were mainly attributed to the variability of single-fiber strength measurements and the assumptions adopted in the analytical strength models. Compression simulations showed satisfactory agreement with the experimental results. The numerical model reproduced the reduction in compressive strength observed in the recycled laminates, although some deviations remained due to mechanisms such as fiber misalignment, local imperfections and interface degradation that are not explicitly included in the analytical formulations.

For the interlaminar shear loading case, the finite element models provide good agreement with the experimental results for the laminates manufactured with virgin carbon fibers. In contrast, a slight overestimation of the maximum load capacity is observed for the recycled CFRP laminates. This discrepancy can be attributed to the higher level of damage and manufacturing-induced imperfections present in the recycled specimens. Furthermore, the relatively small standard deviation predicted by the numerical model reflects the limited influence of the single-fiber input properties. Unlike tensile and compressive loading, the ILSS response is governed primarily by the interlaminar cohesion between adjacent plies and is strongly influenced by manufacturing defects, pre-existing damage, and the through-thickness properties of the laminate.

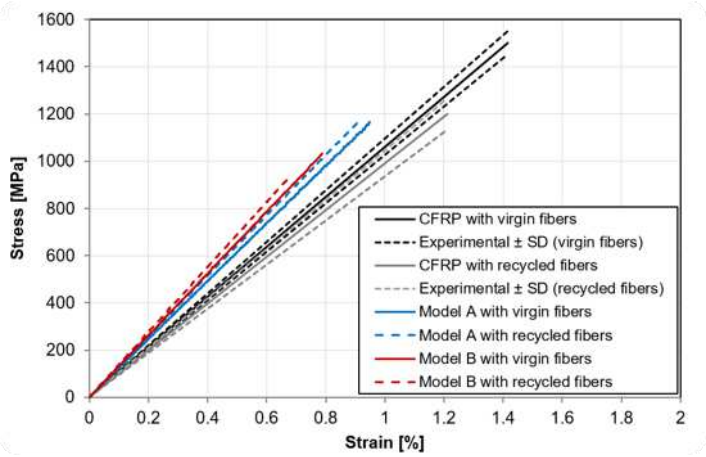

(a)

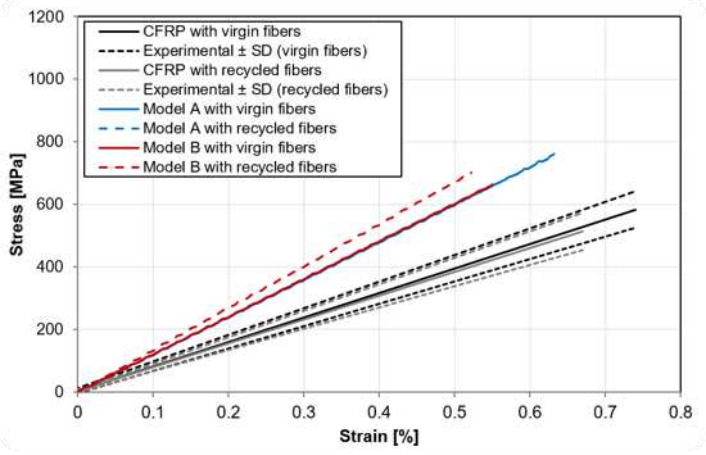

(b)

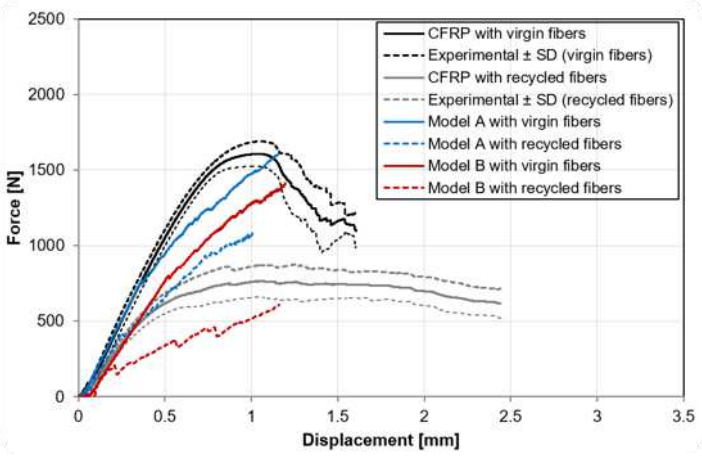

(c)

Fig. 12 Validation of the two modelling approaches (Model A and Model B) against the experimental responses: (a) tension test; (b) compression test; and (c) interlaminar shear strength test.

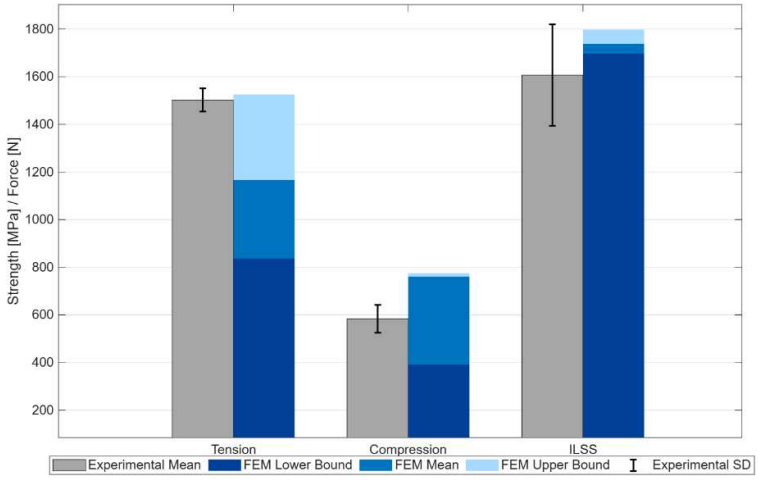

Fig. 13 Comparison between experimental and numerically predicted mechanical properties of CFRP laminates manufactured with virgin carbon fibers.

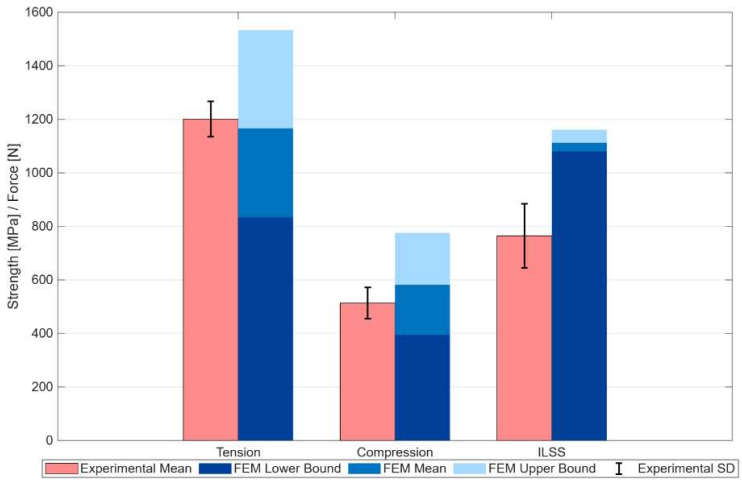

Fig. 14 Comparison between experimental and numerically predicted mechanical properties of CFRP laminates manufactured with recycled carbon fibers.

8. Conclusions

A multiscale framework was developed for predicting the mechanical properties of UD CFRP laminates manufactured with recycled carbon fibers. Application was made for carbon fibers recovered through plasma-assisted solvolysis. The proposed methodology combines single-fiber tensile testing, microbond testing, analytical micromechanical modelling, RVE-based analyses and laminate-level FE analysis. Experimentally measured constituent properties were transferred to the ply scale and then implemented in LS-DYNA laminate models, enabling direct comparison with experimental laminate responses.

For the axial tension, the framework provided good agreement with the experimental results and successfully captured the influence of constituent-property degradation on laminate strength. The analyses demonstrated that the longitudinal tensile properties are governed primarily by the fiber properties, while the fiber–matrix interface remains essential for efficient stress transfer. For the axial compression, satisfactory predictions of laminate strength were obtained, although larger deviations were observed in stiffness. The results indicate that compressive properties are controlled by a combination of fiber, matrix and instability-related failure mechanisms, making it more sensitive to material imperfections that are not represented in numerical models. For the interlaminar shear loading, the initial simulations overpredicted the laminate response due to the assumption of perfect bonding between adjacent plies. The introduction of inter-ply tiebreak interfaces significantly improved the agreement with the experimental results by enabling the simulation of interlaminar damage initiation and propagation. The sensitivity studies further

showed that interface degradation has a greater influence on ILSS performance than reductions in fiber strength.

Nevertheless, both ply-level approaches have limitations: the analytical model (Model A) assumes perfect fiber–matrix bonding and therefore cannot reflect the reduced interfacial strength of the recycled fibers, especially in the transverse and shear strengths, whereas the RVE model (Model B) relies on an idealized periodic fiber arrangement without voids or fiber misalignment and has a higher computational cost. Moreover, neither accounts for the manufacturing-induced damage of the recycled laminates, which explains the overprediction of ILSS.

Overall, the proposed framework successfully transferred constituent-level degradation effects to the laminate scale and provided reliable predictions of the structural response of recycled CFRP laminates. The results confirm that the fiber–matrix interface plays a critical role in the performance of recycled CFRP laminates. Accurate representation of interface degradation is therefore necessary for reliable prediction of laminate behavior and for the development of sustainable composite structures.

Statements and Declarations

Funding No funds, grants, or other support was received.

Competing interests The authors have no relevant financial or non-financial interests to disclose.

Author contributions Ilektra Tourkantoni: Conceptualization, Methodology, Investigation, Formal analysis, Writing – original draft. Konstantinos Tserpes: Supervision, Writing – review and editing. All authors read and approved the final manuscript.

Data availability The data supporting the findings of this study are available from the corresponding author upon reasonable request.

9. References

1. Oliveux, G., Dandy, L.O., Leeke, G.A.: Current status of recycling of fibre reinforced polymers: Review of technologies, reuse and resulting properties. Prog. Mater. Sci. 72, 61–99 (2015). https://doi.org/10.1016/j.pmatsci.2015.01.004
2. Ateeq, M.: A state of art review on recycling and remanufacturing of the carbon fiber from carbon fiber polymer composite. Compos. Part C Open Access. 12, 100412 (2023). https://doi.org/10.1016/j.jcomc.2023.100412

3. Butenegro, J.A., Bahrami, M., Abenojar, J., Martínez, M.Á.: Recent Progress in Carbon Fiber Reinforced Polymers Recycling: A Review of Recycling Methods and Reuse of Carbon Fibers. Materials. 14, 6401 (2021). https://doi.org/10.3390/ma14216401
4. Abdi, B., Wang, Y., Gong, H., Su, M.: Recycling, Remanufacturing and Applications of Semi-Long and Long Carbon Fibre from Waste Composites: A Review. Appl. Compos. Mater. 32, 1237–1265 (2025). https://doi.org/10.1007/s10443-025-10316-6
5. Pickering, S.J.: Recycling technologies for thermoset composite materials—current status. Compos. Part Appl. Sci. Manuf. 37, 1206–1215 (2006). https://doi.org/10.1016/j.compositesa.2005.05.030
6. Pimenta, S., Pinho, S.T.: Recycling carbon fibre reinforced polymers for structural applications: Technology review and market outlook. Waste Manag. 31, 378–392 (2011). https://doi.org/10.1016/j.wasman.2010.09.019
7. Ballout, W., Sallem-Idrissi, N., Sclavons, M., Doneux, C., Bailly, C., Pardoen, T., Van Velthem, P.: High performance recycled CFRP composites based on reused carbon fabrics through sustainable mild solvolysis route. Sci. Rep. 12, 5928 (2022). https://doi.org/10.1038/s41598-022-09932-0
8. Sales-Contini, R.C.M., Costa, H.M.S., Bernardi, H.H., Menezes, W.M.M., Silva, F.J.G.: Mechanical Strength and Surface Analysis of a Composite Made from Recycled Carbon Fibre Obtained via the Pyrolysis Process for Reuse in the Manufacture of New Composites. Materials. 17, 423 (2024). https://doi.org/10.3390/ma17020423
9. Ullah, Z., Kaczmarczyk, Ł., Grammatikos, S.A., Evernden, M.C., Pearce, C.J.: Multi-scale computational homogenisation to predict the long-term durability of composite structures. Comput. Struct. 181, 21–31 (2017). https://doi.org/10.1016/j.compstruc.2016.11.002
10. Liu, Z., Wu, C.T., Ren, B., Liu, W.K., Grimes, R.: Multiscale Simulations of Material with Heterogeneous Structures Based on Representative Volume Element Techniques. 15th Int. -DYNA® Users Conf. (2018)
11. Daniel, I.M., Ishai, O. eds: Engineering mechanics of composite materials. Oxford University Press, New York (2006)
12. Jones, R.M.: Mechanics of composite materials. CRC Press, Taylor & Francis Group, Boca Raton London New York (2021)
13. Vignoli, L.L., Savi, M.A., Pacheco, P.M., Kalamkarov, A.L.: Micromechanical analysis of longitudinal and shear strength of composite laminae. J. Compos. Mater. 54, 4853–4873 (2020). https://doi.org/10.1177/0021998320936343
14. Fiedler, B., Hojo, M., Ochiai, S.: The influence of thermal residual stresses on the transverse strength of CFRP using FEM. Compos. Part Appl. Sci. Manuf. 33, 1323–1326 (2002). https://doi.org/10.1016/S1359-835X(02)00169-0
15. Bu, P., Ruan, W., Liu, J.: Effect of interface and matrix strength on transverse tensile strength of unidirectional CFRP composite. Model. Simul. Mater. Sci. Eng. 31, 065005 (2023). https://doi.org/10.1088/1361-651X/acde93
16. Karkkainen, R., Martinez, O.: Ply Strength Prediction of Unidirectional Continuous Carbon Fiber Composites. Oak Ridge National Laboratory (2023)

17. Rouhi, M.S., Juntikka, M., Landberg, J., Wysocki, M.: Assessing models for the prediction of mechanical properties for the recycled short fibre composites. J. Reinf. Plast. Compos. 38, 454–466 (2019). https://doi.org/10.1177/0731684418824404
18. Brown, K., Brooks, R., Warrior, N.: Numerical Simulation of Damage in Thermoplastic Composite Materials.
19. Albayrak, M., Asan, A.M., Kaman, M.O., Bozkurt, İ.: Experimental and numerical determination of interlayer shear strength of glass fiber-reinforced epoxy composites. J. Struct. Eng. Appl. Mech. 5, (2022). https://doi.org/10.31462/jseam.2022.04289299
20. Perogamvros, N.G., Lampeas, G.N.: Experimental and numerical investigation of AS4/8552 interlaminar shear strength under impact loading conditions. J. Compos. Mater. 50, 2669–2685 (2016). https://doi.org/10.1177/0021998315610899
21. Tan, W., Naya, F., Yang, L., Chang, T., Falzon, B.G., Zhan, L., Molina-Aldareguía, J.M., González, C., Llorca, J.: The role of interfacial properties on the intralaminar and interlaminar damage behaviour of unidirectional composite laminates: Experimental characterization and multiscale modelling. Compos. Part B Eng. 138, 206–221 (2018). https://doi.org/10.1016/j.compositesb.2017.11.043
22. Karuppannan Gopalraj, S., Kärki, T.: A Finite Element Study to Investigate the Mechanical Behaviour of Unidirectional Recycled Carbon Fibre/Glass Fibre–Reinforced Epoxy Composites. Polymers. 13, 3192 (2021). https://doi.org/10.3390/polym13183192
23. Shi, Y., Gillet, A., Mantaux, O., Lacoste, E.: Influence of the architecture on the strength of a unidirectional composite with recycled discontinuous fibres. J. Compos. Mater. 57, 4169–4181 (2023). https://doi.org/10.1177/00219983231205554
24. Aldosari, S.M., AlOtaibi, B.M., Alblalaihid, K.S., Aldoihi, S.A., AlOgab, K.A., Alsaleh, S.S., Alshamary, D.O., Alanazi, T.H., Aldrees, S.D., Alshammari, B.A.: Mechanical Recycling of Carbon Fiber-Reinforced Polymer in a Circular Economy. Polymers. 16, 1363 (2024). https://doi.org/10.3390/polym16101363
25. Tourkantoni, I., Tserpes, K., Marinis, D., Farsari, E., Amanatides, E.: Mechanical Characterization of Carbon Fibers and Their Interfaces Recycled Through Plasma-Assisted Solvolysis Under Different Processing Conditions. https://doi.org/10.3390/fib13120158. (2025)
26. C28 Committee: Test Method for Tensile Strength and Youngs Modulus of Fibers, http://www.astm.org/cgi-bin/resolver.cgi?C1557-14
27. Laurikainen, P., Kakkonen, M., Von Essen, M., Tanhuanpää, O., Kallio, P., Sarlin, E.: Identification and compensation of error sources in the microbond test utilising a reliable high-throughput device. Compos. Part Appl. Sci. Manuf. 137, 105988 (2020). https://doi.org/10.1016/j.compositesa.2020.105988
28. Wang, W., Dai, Y., Zhang, C., Gao, X., Zhao, M.: Micromechanical Modeling of Fiber-Reinforced Composites with Statistically Equivalent Random Fiber Distribution. Materials. 9, 624 (2016). https://doi.org/10.3390/ma9080624
29. Tourkantoni, I., Tserpes, K., Marinis, D., Farsari, E., Amanatides, E., Koutroumanis, N., Pappas, P.N.: Mechanical Behavior of CFRP Laminates Manufactured from Plasma-Assisted Solvolysis Recycled Carbon Fibers. J. Compos. Sci. 10, 49 (2026). https://doi.org/10.3390/jcs10010049

30. D30 Committee: Test Method for Tensile Properties of Polymer Matrix Composite Materials, http://www.astm.org/cgi-bin/resolver.cgi?D3039D3039M-14
31. D30 Committee: Test Method for Compressive Properties of Polymer Matrix Composite Materials with Unsupported Gage Section by Shear Loading, http://www.astm.org/cgi-bin/resolver.cgi?D3410D3410M-03R08
32. D30 Committee: Test Method for Short-Beam Strength of Polymer Matrix Composite Materials and Their Laminates, http://www.astm.org/cgi-bin/resolver.cgi?D2344D2344M-13
33. Liu, W., Huang, H., Cheng, H., Liu, Z.: CFRP Reclamation and Remanufacturing Based on a Closed-loop Recycling Process for Carbon Fibers Using Supercritical N-butanol. Fibers Polym. 21, 604–618 (2020). https://doi.org/10.1007/s12221-020-9575-7
34. Shi, J., Bao, L., Kobayashi, R., Kato, J., Kemmochi, K.: Reusing recycled fibers in high-value fiber-reinforced polymer composites: Improving bending strength by surface cleaning. Compos. Sci. Technol. 72, 1298–1303 (2012). https://doi.org/10.1016/j.compscitech.2012.05.003
35. Liu, L., Huang, Z.: A Note on mori-tanaka's method. Acta Mech. Solida Sin. 27, 234–244 (2014). https://doi.org/10.1016/S0894-9166(14)60033-1
36. Wang, Y., Chen, D., Li, N., Yuan, H., Zhu, Z., Li, Y., Huang, Z.: A micromechanics based elasto-plastic damage model for unidirectional composites under off-axis tensile loads. Sci. Rep. 10, 847 (2020). https://doi.org/10.1038/s41598-020-57771-8
37. Zhou, D., Tong, X., Liu, H., Lv, S., Srivatsan, T.S., Gao, X.: A modified Halpin–Tsai model for predicting the elastic modulus of composite materials. AIP Adv. 14, 015157 (2024). https://doi.org/10.1063/5.0160256
38. Younes, R., Hallal, A., Fardoun, F., Hajj, F.: Comparative Review Study on Elastic Properties Modeling for Unidirectional Composite Materials. In: Hu, N. (ed.) Composites and Their Properties. InTech (2012)
39. Liu, L., Zhang, X., Wang, Z., Wang, Y., Guo, J.: Micromechanics Modeling of Transverse Tensile Strength for Unidirectional CFRP Composite. Materials. 15, 8577 (2022). https://doi.org/10.3390/ma15238577
40. Huang, Z.: Micromechanical prediction of ultimate strength of transversely isotropic composites. Int J Solids Struct. 38, 4147–4172 (2001)
41. Huang, Z.-M.: Simulation of the mechanical properties of fibrous composites by the bridging micromechanics model. Compos. Part Appl. Sci. Manuf. 32, 143–172 (2001). https://doi.org/10.1016/S1359-835X(00)00142-1
42. Sádaba, S., Herráez, M., Naya, F., González, C., Llorca, J., Lopes, C.S.: Special-purpose elements to impose Periodic Boundary Conditions for multiscale computational homogenization of composite materials with the explicit Finite Element Method. Compos. Struct. 208, 434–441 (2019). https://doi.org/10.1016/j.compstruct.2018.10.037
43. Devireddy, S.B.R., Biswas, S.: Effect of Fiber Geometry and Representative Volume Element on Elastic and Thermal Properties of Unidirectional Fiber-Reinforced Composites. J. Compos. 2014, 1–12 (2014). https://doi.org/10.1155/2014/629175
44. Naya, F., González, C., Lopes, C.S., Van Der Veen, S., Pons, F.: Computational micromechanics of the transverse and shear behavior of unidirectional fiber

reinforced polymers including environmental effects. Compos. Part Appl. Sci. Manuf. 92, 146–157 (2017). https://doi.org/10.1016/j.compositesa.2016.06.018
45. Lapczyk, I., Hurtado, J.A.: Progressive damage modeling in fiber-reinforced materials. Compos. Part Appl. Sci. Manuf. 38, 2333–2341 (2007). https://doi.org/10.1016/j.compositesa.2007.01.017
46. Vogiantzi, C., Tserpes, K.: Mechanical properties of carbon fibers and fiber/matrix interface recycled from CFRPs via water/ethanol-based solvolysis under various processing conditions. Eur. J. Mater. 5, 2571803 (2025). https://doi.org/10.1080/26889277.2025.2571803
47. Wang, X., Zhang, J., Wang, Z., Zhou, S., Sun, X.: Effects of interphase properties in unidirectional fiber reinforced composite materials. Mater. Des. 32, 3486–3492 (2011). https://doi.org/10.1016/j.matdes.2011.01.029
48. Camanho, P.P., Davila, C.G., De Moura, M.F.: Numerical Simulation of Mixed-Mode Progressive Delamination in Composite Materials. J. Compos. Mater. 37, 1415–1438 (2003). https://doi.org/10.1177/0021998303034505
49. Turon, A., Camanho, P.P., Costa, J., Dávila, C.G.: A damage model for the simulation of delamination in advanced composites under variable-mode loading. Mech. Mater. 38, 1072–1089 (2006). https://doi.org/10.1016/j.mechmat.2005.10.003

Appendix A. Micromechanical Models

This appendix presents the analytical micromechanical models used in Section 4.1 to estimate the elastic constants of the UD ply from the properties of its constituents. In all models, direction 1 is the fiber direction and the 2–3 plane is the transverse plane; the fibers are transversely isotropic and the matrix is isotropic. The subscripts f, m and c denote the fiber, the matrix and the interphase, respectively.

A.1. Mori–Tanaka Model

The Mori–Tanaka model estimates the elastic properties of fiber-reinforced composites, assuming that the fibers are transversely isotropic and embedded in an isotropic matrix. The composite is treated as a two-phase material consisting of infinitely long cylindrical fibers within an infinite matrix [35]. Using the 3D Mori–Tanaka tensor, the elastic constants of the composite are calculated from the properties of the fiber and the matrix, namely the longitudinal and transverse moduli, the shear moduli and the Poisson's ratios (Equations (A1)–(A9)). A_{ij} are the components of the Mori–Tanaka strain-concentration tensor.

$$A_{11} = \frac{E_m}{E_{1,f}}\left(1 + \frac{\nu_m\left(\nu_m - \nu_{12,f}\right)}{(1+\nu_m)(1-\nu_m)}\right) \tag{A1}$$

$$A_{12} = A_{13} = \frac{E_m}{E_{2,f}} \frac{\nu_m(1-\nu_{23,f})}{2(1+\nu_m)(1-\nu_m)} - \frac{E_m}{E_{1,f}} \frac{\nu_{12,f}}{(1+\nu_m)(1-\nu_m)} + \frac{\nu_m}{2(1-\nu_m)} \tag{A2}$$

$$A_{21} = A_{31} = \frac{E_m}{E_{1,f}} \frac{\nu_m - \nu_{12,f}}{2(1+\nu_m)(1-\nu_m)} \tag{A3}$$

$$A_{22} = A_{33} = \frac{E_m}{E_{2,f}} \frac{\nu_{23,f} - 3}{8(\nu_m - 1)(\nu_m + 1)} + \frac{E_m}{E_{1,f}} \frac{\nu_{12,f}\nu_m}{2(\nu_m - 1)(\nu_m + 1)} + \frac{(\nu_m + 1)(4\nu_m - 5)}{8(\nu_m - 1)(\nu_m + 1)} \tag{A4}$$

$$A_{32} = A_{23} = \frac{E_m}{E_{2,f}} \frac{3\nu_{23,f} - 1}{8(\nu_m - 1)(\nu_m + 1)} + \frac{E_m}{E_{1,f}} \frac{\nu_{12,f}\nu_m}{2(\nu_m - 1)(\nu_m + 1)} + \frac{(\nu_m + 1)(1 - 4\nu_m)}{8(\nu_m - 1)(\nu_m + 1)} \tag{A5}$$

$$A_{44} = \frac{G_m}{G_{23,f}} \frac{1}{4(1-\nu_m)} + \frac{3 - 4\nu_m}{4(1-\nu_m)} \tag{A6}$$

$$A_{55} = A_{66} = \frac{G_m + G_{12,f}}{2G_{12,f}} \tag{A7}$$

$$S_{11,f} = \frac{1}{E_{1,f}}, \quad S_{12,f} = S_{21,f} = S_{13,f} = S_{31,f} = -\frac{\nu_{12,f}}{E_{1,f}},$$

$$S_{23,f} = S_{32,f} = -\frac{\nu_{23,f}}{E_{2,f}}, \tag{A8}$$

$$S_{22,f} = S_{33,f} = \frac{1}{E_{2,f}}, \qquad S_{44,f} = \frac{1}{G_{23,f}}, \qquad S_{55,f} = S_{66,f} = \frac{1}{G_{12,f}}$$

$$S_{11,m} = S_{22,m} = S_{33,m} = \frac{1}{E_m},$$

$$S_{44,m} = S_{55,m} = S_{66,m} = \frac{1}{G_m}, \tag{A9}$$

$$S_{12,m} = S_{21,m} = S_{13,m} = S_{31,m} = S_{23,m} = S_{32,m} = -\frac{\nu_m}{E_m},$$

where $S_{ij,f}$ and $S_{ij,m}$ are the components of the compliance matrices of the fiber and the matrix. After the compliance matrices of the fiber and the matrix are determined, the auxiliary constants b_1–b_5 are defined in order to facilitate the calculation of the ply elastic constants E_1, E_2, G_{12}, G_{23} and ν_{12}, the longitudinal and transverse moduli, the in-plane and transverse shear moduli and the Poisson's ratio of the ply, respectively, (Equations (A10)–(A25)). The volume fractions of the fiber

and the matrix are related by $V_f + V_m = 1$. The ply properties are obtained by equating the overall composite compliance with that of the equivalent transversely isotropic ply.

$$b_1 = V_f V_m\left[A_{12}\left(S_{12,m} - S_{12,f}\right) + A_{11}\left(S_{22,f} + S_{11,m}\right)\right] \tag{A10}$$

$$b_2 = V_f^2\left(S_{22,f} + S_{11,m}\right) - 2A_{12}A_{21}S_{11,m}V_m^2 \tag{A11}$$

$$b_3 = A_{21}V_m\left[2A_{32}S_{11,m}V_m - V_f\left(S_{22,f} - S_{23,f} + S_{11,m} + S_{12,m}\right)\right] \tag{A12}$$

$$b_4 = V_f\left(S_{12,m} - S_{12,f}\right)\left(V_f - A_{32}V_m\right) \tag{A13}$$

$$b_5 = A_{32}V_f V_m\left(S_{12,m} - S_{23,f}\right) - A_{32}^2 S_{11,m}V_m^2 + S_{22,f}V_f^2 \tag{A14}$$

$$E_1^{num} = (A_{11} + A_{22} + A_{32})V_f V_m + [A_{11}(A_{22} + A_{32}) - 2A_{12}A_{21}]V_m^2 + V_f^2 \tag{A15}$$

$$\begin{aligned} E_1^{den} = {} & V_f V_m\left[2A_{21}\left(S_{12,m} - S_{12,f}\right) + (A_{22} + A_{32})S_{11,f} + A_{11}S_{11,m}\right] \\ & + [A_{11}(A_{22} + A_{32}) - 2A_{12}A_{21}]V_m^2 S_{11,m} + V_f^2 S_{11,f} \end{aligned} \tag{A16}$$

$$E_1 = \frac{E_1^{num}}{E_1^{den}} \tag{A17}$$

$$E_2^{num} = \left[(A_{22} - A_{32})V_m + V_f\right]E_1^{num} \tag{A18}$$

$$\begin{aligned} E_2^{den} = {} & A_{22}(b_1 + b_2)V_m + A_{12}(b_3 + b_4)V_m + b_5\left(A_{11}V_m + V_f\right) \\ & + A_{22}^2 S_{11,m}V_m^2\left(A_{11}V_m + V_f\right) \end{aligned} \tag{A19}$$

$$E_2 = \frac{E_2^{num}}{E_2^{den}} \tag{A20}$$

$$G_{12} = \frac{\left(V_f + V_m A_{66}\right)G_{12,f}G_m}{V_f G_m + V_m A_{66}G_{12,f}} \tag{A21}$$

$$G_{23} = \frac{\left(V_f + V_m A_{44}\right)G_{23,f}G_m}{V_f G_m + V_m A_{44}G_{23,f}} \tag{A22}$$

$$\begin{aligned} \nu_{12}^{num} = {} & A_{12}V_m\left[V_f\left(S_{11,f} - S_{11,m}\right) + 2A_{21}V_m S_{12,m}\right] \\ & - \left(V_f + A_{11}V_m\right)\left[V_f S_{12,f} + (A_{22} + A_{32})V_m S_{12,m}\right] \end{aligned} \tag{A23}$$

$$\begin{aligned} \nu_{12}^{den} = {} & V_f^2 S_{11,f} + [A_{11}(A_{22} + A_{32}) - 2A_{12}A_{21}]V_m^2 S_{11,m} \\ & + V_f V_m\begin{bmatrix}(A_{22} + A_{32})S_{11,f} + A_{11}S_{11,m} + \\ 2A_{21}\left(S_{12,m} - S_{12,f}\right)\end{bmatrix} \end{aligned} \tag{A24}$$

$$\nu_{12} = \frac{\nu_{12}^{num}}{\nu_{12}^{den}} \tag{A25}$$

A.2. Bridging Model

The Bridging model is a three-phase approach that explicitly accounts for the matrix, the reinforcement and the interphase. It captures the nonlinearity of the composite and the elastoplastic behavior of the matrix, while maintaining a simplified linear elastic framework. The method involves two sub-systems: the fibers and the interphase are first treated as a biphasic subsystem (equivalent fiber) and are then combined with the matrix into a three-phase composite.

The compliance matrices of the fiber, the interphase and the matrix are combined using the bridging relations (Equations (A26)–(A39)), and the overall ply properties are calculated from the compliance matrix of the resulting system. The interphase is assumed isotropic and the fibers transversely isotropic. The compliance matrix of the equivalent fiber is:

$$[M^{ef}] = \left(\frac{V_f}{V_f + V_c}[M^f] + \frac{V_c}{V_f + V_c}[M^c][A^I]\right)\left(\frac{V_f}{V_f + V_c}[I] + \frac{V_c}{V_f + V_c}[A^I]\right)^{-1}, \tag{A26}$$

where $[I]$ is the identity matrix and $[M^c]$ is the compliance matrix of the interphase,

$$[M^c] = \begin{bmatrix} M_{11}^c & M_{12}^c & M_{13}^c & 0 & 0 & 0 \\ M_{21}^c & M_{22}^c & M_{23}^c & 0 & 0 & 0 \\ M_{31}^c & M_{32}^c & M_{33}^c & 0 & 0 & 0 \\ 0 & 0 & 0 & M_{44}^c & 0 & 0 \\ 0 & 0 & 0 & 0 & M_{55}^c & 0 \\ 0 & 0 & 0 & 0 & 0 & M_{66}^c \end{bmatrix} \tag{A27}$$

$$\begin{aligned} M_{11}^c = M_{22}^c = M_{33}^c = \frac{1}{E_c}, \qquad & M_{12}^c = M_{21}^c = M_{13}^c = M_{31}^c = M_{23}^c = M_{32}^c \\ & = -\frac{\nu_c}{E_c}, \qquad M_{44}^c = M_{55}^c = M_{66}^c = \frac{1}{G_c} \end{aligned} \tag{A28}$$

E_c, G_c and ν_c are the elastic modulus, the shear modulus and the Poisson's ratio of the interphase material. The compliance matrix of the fiber, $[M^f]$, has the same form as $[M^c]$, with:

$$\begin{aligned} M_{11}^f &= \frac{1}{E_{1,f}}, \qquad M_{12}^f = M_{21}^f = M_{13}^f = M_{31}^f = -\frac{\nu_{12,f}}{E_{1,f}}, \qquad M_{23}^f = M_{32}^f = -\frac{\nu_{23,f}}{E_{2,f}}, \\ M_{22}^f &= M_{33}^f = \frac{1}{E_{2,f}}, \qquad M_{44}^f = \frac{1}{G_{23,f}}, \qquad M_{55}^f = M_{66}^f = \frac{1}{G_{12,f}} \end{aligned} \tag{A29}$$

The bridging matrix $[A^I]$ of the fiber–interphase subsystem is:

$$[A^I] = \begin{bmatrix} A_{11}^I & A_{12}^I & A_{13}^I & 0 & 0 & 0 \\ 0 & A_{22}^I & 0 & 0 & 0 & 0 \\ 0 & 0 & A_{33}^I & 0 & 0 & 0 \\ 0 & 0 & 0 & A_{44}^I & 0 & 0 \\ 0 & 0 & 0 & 0 & A_{55}^I & 0 \\ 0 & 0 & 0 & 0 & 0 & A_{66}^I \end{bmatrix} \tag{A30}$$

$$A_{11}^I = \frac{E_c}{E_{1,f}},\ A_{22}^I = A_{33}^I = A_{44}^I = \beta + (1-\beta)\frac{E_c}{E_{2,f}},$$

$$A_{55}^I = A_{66}^I = \alpha + (1-\alpha)\frac{G_c}{G_{12,f}}, \tag{A31}$$

$$A_{12}^I = A_{13}^I = (A_{11}^I - A_{22}^I)\frac{M_{12}^f - M_{12}^c}{M_{11}^f - M_{11}^c},$$

where M_{11}^c, M_{12}^c, M_{11}^f and M_{12}^f are the elements of the compliance matrices of the interphase and the fiber, respectively. According to the literature, the recommended values for Bridging parameters α and β are 0.3 [41]. For the overall composite, the compliance matrix is obtained by bridging the equivalent fiber with the matrix:

$$[M] = \Big((V_f + V_c)[M^{ef}] + V_m[M^m][A^{II}]\Big)\Big((V_f + V_c)[I] + V_m[A^{II}]\Big)^{-1} \tag{A32}$$

The matrix $[M^m]$ contains the elastic constants of the matrix, which is treated as an isotropic material, and has the same form as $[M^c]$, with:

$$M_{11}^m = M_{22}^m = M_{33}^m = \frac{1}{E_m},$$
$$M_{12}^m = M_{21}^m = M_{13}^m = M_{31}^m = M_{23}^m = M_{32}^m = -\frac{\nu_m}{E_m}, \tag{A33}$$
$$M_{44}^m = M_{55}^m = M_{66}^m = \frac{1}{G_m}$$

$[A^{II}]$ is the bridging matrix of the overall two-phase system. It has the same form as $[A^I]$ and is defined as:

$$A_{11}^{II} = \frac{E_m}{E_1^{ef}}, \qquad A_{22}^{II} = A_{33}^{II} = A_{44}^{II} = \beta + (1-\beta)\frac{E_m}{E_2^{ef}}, \tag{A34}$$

$$A_{55}^{II} = A_{66}^{II} = \alpha + (1-\alpha)\frac{G_m}{G_{12}^{ef}},$$

$$A_{12}^{II} = A_{13}^{II} = (A_{11}^{II} - A_{22}^{II})\frac{M_{12}^{ef} - M_{12}^{m}}{M_{11}^{ef} - M_{11}^{m}},$$

where E_1^{ef}, E_2^{ef} and G_{12}^{ef} are the longitudinal modulus, the transverse modulus and the shear modulus of the equivalent fiber, which are determined from $[M^{ef}]$ as:

$$E_1^{ef} = \frac{1}{M_{11}^{ef}}, \qquad E_2^{ef} = \frac{1}{M_{22}^{ef}}, \qquad G_{12}^{ef} = \frac{1}{M_{66}^{ef}} \tag{A35}$$

Finally, the ply constants are calculated by equating the coefficients of the compliance matrix of the overall composite with the corresponding coefficients of the compliance matrix of a transversely isotropic ply:

$$\frac{1}{E_1} = M_{11}, \qquad \frac{1}{E_2} = M_{22}, \qquad \frac{1}{G_{23}} = M_{44}, \qquad \frac{1}{G_{12}} = M_{55}, \qquad -\frac{\nu_{12}}{E_1} = M_{12}, \tag{A36}$$

where E_1 and E_2 are the longitudinal and transverse moduli, and G_{12}, G_{23} and ν_{12} are the in-plane and transverse shear moduli and the Poisson's ratio of the ply, respectively. The Poisson's ratio ν_{12} can equivalently be calculated from the rule of mixtures of the equivalent fiber and the matrix (Equation (A37)), where ν_{12}^{ef} is determined for the equivalent system of the fiber and the interphase (Equations (A38)–(A39)):

$$\nu_{12} = (V_f + V_c)\nu_{12}^{ef} + V_m\nu_m \tag{A37}$$

$$\nu_{12}^{ef} = V_f^{eff}\nu_{12,f} + V_c^{eff}\nu_c \tag{A38}$$

$$V_f^{eff} = \frac{V_f}{V_f + V_c}, \qquad V_c^{eff} = \frac{V_c}{V_f + V_c} \tag{A39}$$

A.3. Improved Halpin–Tsai Model

The improved Halpin–Tsai model extends the traditional Halpin–Tsai method, which neglects the interphase, by treating the composite as a three-phase material (fiber, matrix and interphase). The fiber and the interphase are first combined into an equivalent fiber, which is then combined with the matrix. The fibers are considered transversely isotropic, the matrix and the interphase isotropic, and the behavior linear elastic. The ply properties are calculated from the properties and volume

fractions (C_f, C_m, C_c) of the fiber, the matrix and the interphase, with $C_f = V_f$ and $C_f + C_m + C_c = 1$ (Equations (A40)–(A43)):

$$E_1 = E_f C_f + E_m C_m + E_c C_c \tag{A40}$$

$$E_2 = E_m \frac{b_E \xi C_m + \theta_E (1 + \xi - \xi C_m) \frac{E_c}{E_m}}{b_E (\xi + 1 - C_m) + \theta_E C_m \frac{E_c}{E_m}} \tag{A41}$$

$$\nu_{12} = \nu_{12,f} C_f + \nu_m C_m + \nu_c C_c \tag{A42}$$

$$G_{12} = G_m \frac{b_G \xi C_m + \theta_G (1 + \xi - \xi C_m) \frac{G_c}{G_m}}{b_G (\xi + 1 - C_m) + \theta_G C_m \frac{G_c}{G_m}} \tag{A43}$$

E_f and G_f are the averages of the elastic and shear moduli of the fiber over the three directions, and the interphase properties (E_c, G_c, ν_c) are taken as the average of the fiber and matrix properties. The parameter ξ is taken equal to 3.4 [37], and

$$\begin{aligned} b_E &= \xi + 1 - C_c + C_c \frac{E_f}{E_c}, & b_G &= \xi + 1 - C_c + C_c \frac{G_f}{G_c}, \\ \theta_E &= \xi C_c + (1 + \xi - \xi C_c) \frac{E_f}{E_c}, & \theta_G &= \xi C_c + (1 + \xi - \xi C_c) \frac{G_f}{G_c}, \end{aligned} \tag{A44}$$

where b_E, b_G, θ_E and θ_G are auxiliary parameters. The interphase volume fraction C_c is computed from the fiber radius r_f and the outer radius of the interphase r_i:

$$\frac{C_c}{C_c + C_f} = \frac{r_i^2 - r_f^2}{r_i^2}, \tag{A45}$$

where $r_f = 3.5$ µm and $r_i = 3.7$ µm, since the fiber has a diameter of 7 µm and the interphase a thickness of 200 nm.

A.4. Chamis Model

The Chamis model is based on the rule of mixtures and provides a simple linear estimation of the longitudinal modulus of the ply between the fiber and matrix values. The transverse modulus is dominated by the matrix, while the contribution of the fibers is minor. The shear stresses are assumed equal in the fiber and the matrix, and linear elastic behavior is considered [38]. The ply properties are calculated as:

$$E_1 = E_{1,f} V_f + E_m V_m \tag{A46}$$

$$E_2 = \frac{E_m}{V_m + V_f\, E_m/E_{2,f}} \tag{A47}$$

$$\nu_{12} = \nu_{12,f} V_f + \nu_m V_m \tag{A48}$$

$$G_{12} = \frac{G_m}{V_m + V_f\, G_m/G_{12,f}} \tag{A49}$$